

A Plastic Boundary Layer in Wedge Indentation of Aluminum

Tatsuya Sugihara^{1,*}, Anirudh Udupa² and Koushik Viswanathan³

¹Department of Mechanical Engineering, Osaka University, Osaka 565-0871, Japan

²School of Industrial Engineering Purdue University, West Lafayette, IN 47907, USA

³Department of Mechanical Engineering, Indian Institute of Science, Bengaluru, 560012, India

We study plastic flow in the vicinity of an indenter-material interface in wedge indentation of aluminum using high speed *in situ* imaging and particle image velocimetry (PIV) analysis. Displacement and strain fields in the indentation zone are obtained at high-resolution for different indenter angles and two lubrication conditions. These fields can be used to demarcate essential features of the material flow phenomena. The deformed layers close to the indenter wall fit a classical boundary layer profile in the framework of a Bingham-solid. Equivalent Bingham viscosities and boundary layer scaling relations are obtained. The viscosity values appear to reflect the nature of the friction interaction at the indenter-material interface and can potentially be used as a discriminating parameter for evaluating contributions to deformation and dissipation arising from interface friction. [doi:10.2320/matertrans.MD201907]

(Received January 8, 2019; Accepted January 30, 2019; Published March 15, 2019)

Keywords: boundary-layer, *in situ* imaging, metals, plasticity, interface friction

1. Introduction

Tool/die-material interfaces in machining and deformation processing are characterized by severe conditions of stress and temperature (Fig. 1), quite different from conventional engineering sliding contacts. These conditions have a major influence on surface deformation fields, process energy and product quality. In metal-cutting, severe friction and friction-induced deformation lead to a “secondary shear zone” at the tool-chip interface, thus causing a high cutting temperature and cutting force.¹⁻⁵ The effects of this secondary deformation are quite significant, influencing cutting tool life and finished surface quality.^{1,3} Similar friction-induced deformation, so-called “redundant deformation”, arises also at die-workpiece interfaces in forming processes, such as sheet forming, bulk deformation processing, microforming, and incremental forming.⁶⁻⁸ The die-workpiece contact condition and associated frictional deformation exhibit a major, often adverse, effect on product surface quality attributes such as roughness, defects, residual strains, and stresses.^{9,10} Despite the above-mentioned criticality of interface friction and frictional deformation at the contact in metal processing, it has been difficult to predict the nature of these severe friction conditions using conventional friction models, such as Coulomb friction, sticking friction, or mixed Coulomb-sticking friction models.^{1,11-13} The complexities of the friction conditions are in large part due to extremely high normal and shear stresses, nascent surfaces, intimate contact, and sometimes high-temperature and high sliding speed. In particular, the high normal loads cause the real area of contact to equal the apparent area of contact, thereby causing the contact condition to differ from conventional engineering sliding contacts (e.g., bearings, piston-cylinder).

In such severe sliding contacts, it has been reported that a localization of material flow occurs in the vicinity of the friction interface, likely due to friction induced retardation of material flow close to the tool face.^{1-3,11-14} Examples of such material flow patterns in the cutting and rolling processes are

shown in Fig. 1. Here, severe friction at tool-chip (Fig. 1(a)) and die-workpiece (Fig. 1(b)) interfaces causes the velocity difference between the bulk of the chip and the secondary shear zone, or between the bulk of the workpiece and the redundant deformation zone, respectively. The resultant flow patterns resemble a “boundary” or “wall” layer, akin to the layer that forms when a fluid is forced to flow over a flat plate.^{5,15} This suggests that the friction-induced deformation field could be a plastic boundary layer, and that the phenomenological characterization of the boundary layer could provide various insights into the complex nature of friction in contacts under extreme conditions. Although it is clear that an understanding of this plastic boundary layer would require detailed measurement of the displacement field close to interfaces, it is extremely difficult to quantitatively investigate it using conventional method, such as a quick stop test^{5,16} or the visio-plasticity method¹⁷ because the region of high deformation is typically extremely thin.

The present study explores this wall layer using indentation of metals as a model system representative of deformation processes involving extremely high-normal and shear loads. Using direct *in situ* observations of the deformation coupled with high-speed imaging and particle image velocimetry techniques (PIV), displacement, velocity, and strain fields are obtained for different indenter angles and lubrication conditions. Particular attention is focused on the deformation that is very close to the indenter interface and the characteristics of this wall layer. This wall flow pattern is compared with a classical boundary layer model for a Bingham-type viscoplastic solid. The results support the hypothesis of the wall layer being a boundary layer.

2. Experimental Details

2.1 Experimental setup

Wedge indentation experiments on annealed aluminum 1100 (hardness = 23 HV) were conducted under conditions of plane-strain. As shown in Fig. 2, plain strain was ensured by clamping against the specimen, a thick, transparent glass block, which restricts out-of-plane deformation. Wedge-

*Corresponding author, E-mail: t-sugihara@mech.eng.osaka-u.ac.jp

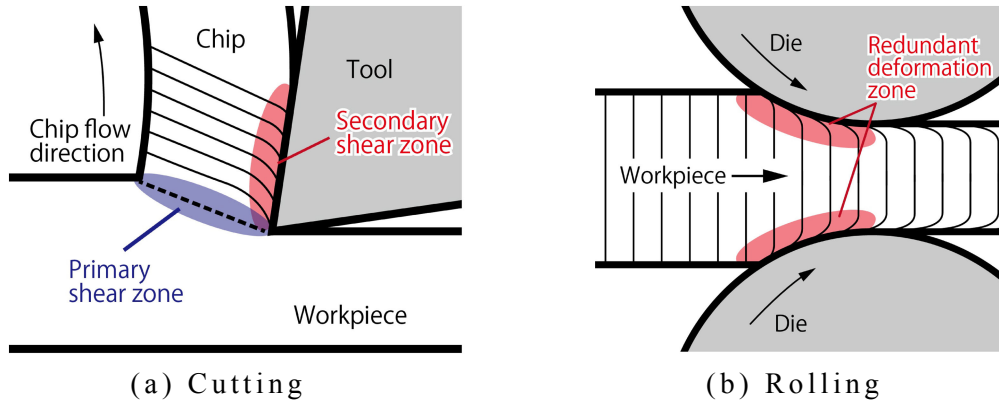


Fig. 1 Schematic of friction-induced material flow in metal processing; (a) Secondary shear zone in cutting and (b) Redundant deformation zone in rolling.

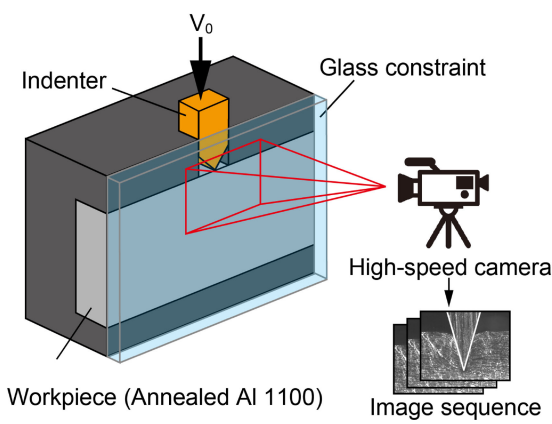


Fig. 2 Experimental setup for *in situ* imaging and observations of wedge-indentation.

shaped indenters (high-speed steel) with apical angles (α_0) of 30°, 60°, 90°, and 120° were used for the indentation. The indentation was performed at a constant indentation speed (V_0) of 1.0 mm/s, during which the indentation force in the vertical direction was measured using a piezoelectric dynamometer (Kistler 9272, natural frequency ~ 2 kHz) onto which the workpiece was mounted. The material flow in the vicinity of the indenter-workpiece interface was recorded *in situ* using a high-speed CMOS camera (PCO dimax) coupled to a long working distance microscope objective. Images were captured at 500 frames per second and at a

spatial resolution of 1.4 μm per pixel. The image sequences were analyzed using a digital image correlation technique—Particle Image Velocimetry (PIV)—to obtain the quantitative details of flow, such as flow line patterns and effective (von Mises) strain fields.^{18–20} This data enabled detailed mapping of the underlying surface plastic flow modes.

2.2 Image analysis procedures

Figure 3 shows an image sequence with superimposed (deformed) grid lines from PIV captured at 0.2-second intervals ($\alpha_0 = 30^\circ$). The (initial) grid lines at $t = t_0$, albeit virtual, were placed orthogonal to the wedge face (Fig. 3(a)). The x and y axes are tangential and normal to the indenter face, respectively, with the origin fixed at the indenter tip. The distortion of the grid lines $U_n(y, t)$ (n : line number) provides a measure of the deformation of the material. Figure 4 shows the displacement field $U_n(y, t_0 + 0.5 \text{ s})$ obtained from Fig. 3(d). Subsequently, the displacement field was normalized by dividing by the corresponding displacement magnitude $U_n(y, t)/U_{n \text{ max}}(t)$, where $U_{n \text{ max}}(t)$ is the displacement far from the indenter face obtained by $U_n(\infty, t) - U_n(0, t)$. Figure 5 shows the normalized displacement fields at $t = t_0 + 0.1 \text{ s}$, $t_0 + 0.3 \text{ s}$, and $t_0 + 0.5 \text{ s}$. As shown in this figure, the normalized displacement fields at each instant of time have almost the same shape, indicating that the material flow along the indenter face has a constant velocity field during the indentation process. Furthermore, the dots superimposed on the flow lines in Fig. 3(d)

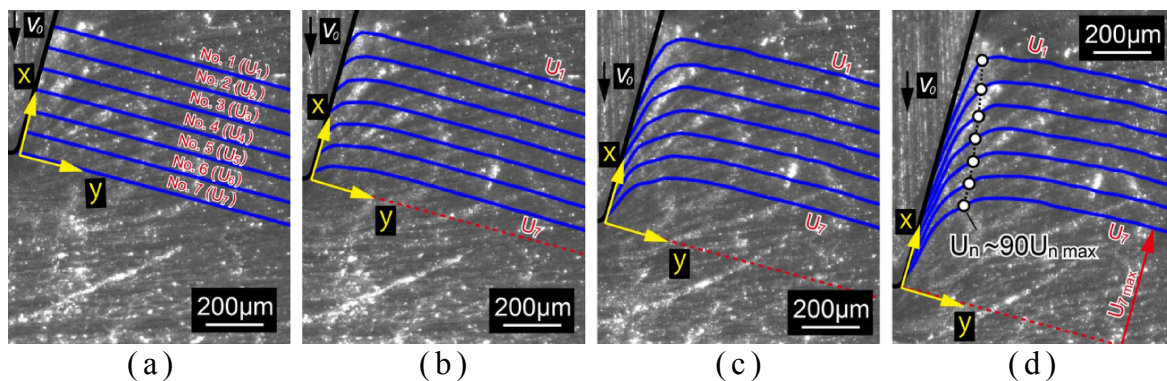


Fig. 3 Development of material flow in the indenter vicinity, as revealed by four frames from a high-speed image sequence and PIV analysis ($\alpha_0 = 30^\circ$). (a) $t = t_0$, (b) $t = t_0 + 0.1 \text{ s}$, (c) $t = t_0 + 0.3 \text{ s}$, (d) $t = t_0 + 0.5 \text{ s}$.

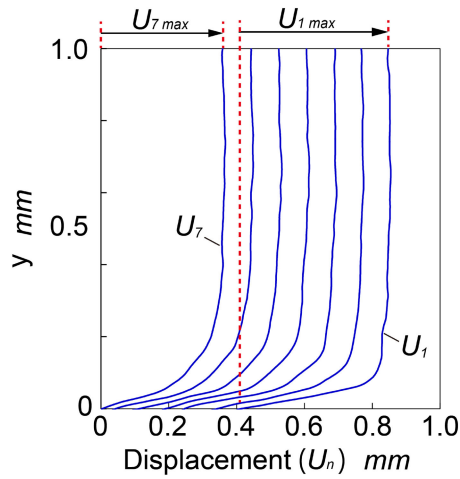


Fig. 4 Displacement field in indentation zone, including wall vicinity, for apical angle = 30° ($t = t_0 + 0.5$ s).

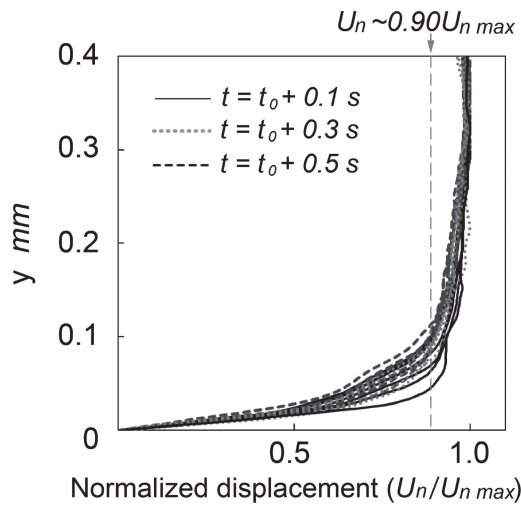


Fig. 5 Normalized displacement field ($U_n(y, t)/U_{n \max}(t)$) at $t = t_0 + 0.1$ s, $t_0 + 0.3$ s, and $t_0 + 0.5$ s ($\alpha_0 = 30^\circ$).

correspond to points with $U_n \sim 90\%U_{n \max}$ at $t = t_0 + 0.5$ s; they are used to define the thickness of the wall (subsequently boundary layer) layer along the wedge indenter in the present study.

Similarities between the solid wall- and fluid boundary-layers may now be identified. The wall layer associated with the plastic flow is visually evident; it is similar to a laminar fluid boundary layer with steep velocity gradients.²¹⁾ Similar to viscous dissipation in fluids, plastic dissipation is primarily confined to the wall layer and the motion outside the wall-region is primarily rigid body motion.

3. Results and Discussions

3.1 Modes of deformation

Figure 6 shows the material flow lines and the corresponding normalized displacement field at $t = t_0 + 0.5$ s for the 60°, 90°, and 120° indenters, respectively. For the apical angles of 60° (Fig. 6(a)) and 90° (Fig. 6(b)), the deformation is confined mainly to a region close to the indenter face as with the case of the narrowest-angle (30°) indenter (Fig. 3(d)). In particular, the flow lines in the area adjacent to

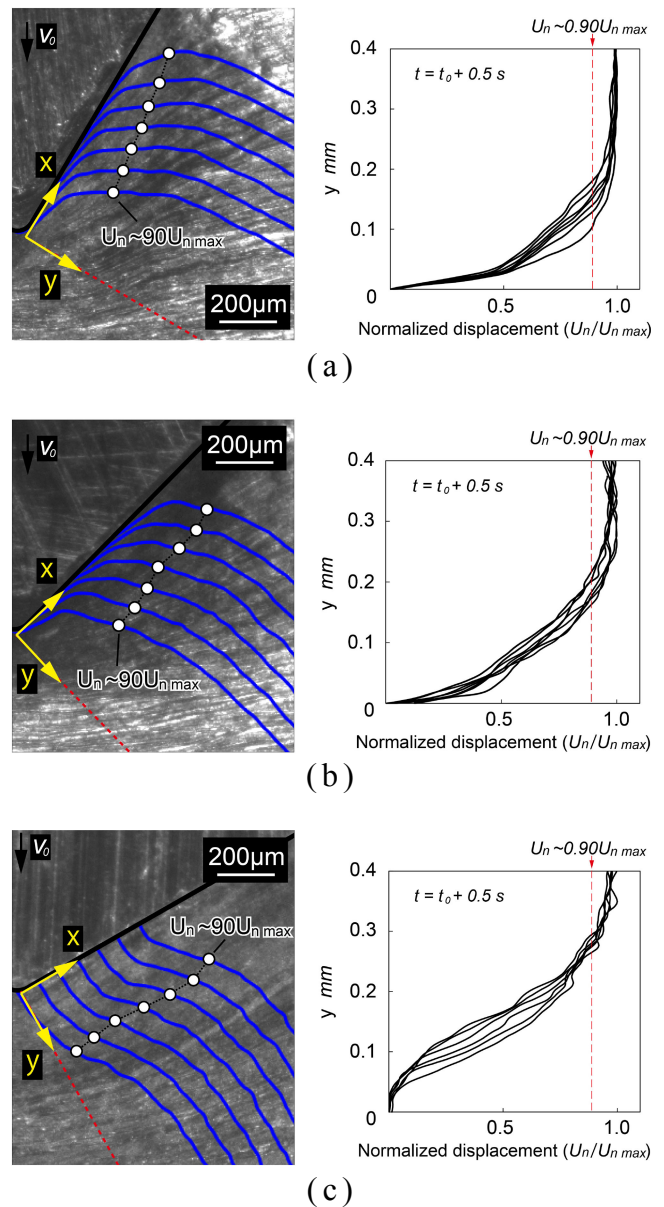


Fig. 6 Material flow lines (left) and the corresponding normalized displacement fields (Right). The dots superimposed on the displacement fields indicates the points where U_n reaches a value equal to 90% $U_{n \max}$. (a) $\alpha_0 = 60^\circ$, (b) $\alpha_0 = 90^\circ$, (c) $\alpha_0 = 120^\circ$.

the indenter face are tangential to the indenter face because the workpiece material is dragged by the interface friction between the indenter and workpiece. In contrast, the material flow with the widest-angle (120°) indenter (Fig. 6(c)) is quite different from those of the other indenters. Here, the flow lines continue to remain normal to the indenter face in the wall-region of the indenter during the indentation process, resulting in the normalized displacement field with an “S-shape”. Obviously, there is no wall-layer with steep velocity gradients along the indenter face in this case.

These differences clearly indicate a transition from a “cutting mode” of deformation to a “radial compression mode” with increasing indenter apex angle. It has been reported that the cutting mode can be characterized by a deformation zone that is confined to a very small region just underneath the indenter, whereas the radial compression

mode leads to a deformation zone that extend over a large area beneath the indenter.^{22–24}) This transition has been confirmed by systematic analysis of velocity fields and other deformation field attributes, see companion paper submitted.²⁵⁾

Here we just capture the transition from the cutting to the radial-compression mode using strain fields. Because the PIV analysis provides a small displacement field in each frame, the incremental effective (von Mises) strain ($d\epsilon_{eff}$) field imposed in each frame can be obtained as

$$\begin{aligned} d\epsilon_{xx} &= \frac{\partial u_x}{\partial x}, \\ d\epsilon_{yy} &= \frac{\partial u_y}{\partial y}, \\ d\epsilon_{xy} &= \frac{1}{2} \left(\frac{\partial u_x}{\partial y} + \frac{\partial u_y}{\partial x} \right), \\ d\epsilon_{eff} &= \sqrt{\frac{2}{3} (d\epsilon_{xx}^2 + d\epsilon_{yy}^2 + 2d\epsilon_{xy}^2)} \end{aligned} \quad (1)$$

where u_x and u_y are the displacement components in the x and y directions, respectively. Therefore, the total effective strain value (ϵ_{eff}) at different locations and various stages of the indentation can be calculated by integrating the incremental strain along the particle trajectories.¹⁹⁾

Figure 7 shows the strain fields for each indenter at $t = t_0 + 0.5$ s. When using the narrow-angle indenters, such as the 30° (Fig. 7(a)) and 60° (Fig. 7(b)), extreme strain localization in the vicinity of the indenter face is evident, suggesting that the friction-induced deformation is dominant at the interface. However, the strain localization becomes significantly less and the strain field becomes more diffuse

with increasing apical angle (Figs. 7(c) and (d)). This result also confirms that the deformation zone extends over a large area beneath the indenter in the radial compression mode deformation.

Given the nature of the observed material flow, it was decided to examine in greater detail the deformation in the wall region with the narrow-angle (30°) indenter in the context of interface friction. This is where friction effects should be expected to be important since there was a significant material velocity component parallel to the wall and associated strained layer.

3.2 Boundary layer in friction-induced deformation

Figure 8 shows the thickness of the wall layers ($t = t_0 + 0.5$ s) at different indentation speeds ($V_0 = 0.1, 1.0,$ and 2.0 mm/s) for the 30° indenter where the strain localization at the wall is most intense. The thickness of the wall layers decreases with increasing indentation speed, suggesting that the deformation at the indenter wall becomes increasingly localized with increasing indentation speed. This result implies that the material at the sliding interface behaves similar to that typically observed in a viscous fluid flowing past a solid surface.²⁶⁾ If we treat the deformation in the region close to the indenter wall as that of a Bingham solid, then the following constitutive law holds

$$\tau = \theta + \mu \left(\frac{\partial u}{\partial y} \right) \quad (2)$$

where τ is the material flow strength, θ is static shear flow stress, and μ is the dynamic viscosity coefficient. Such a law is sometimes used to describe a metal plasticity at relatively high strain rates ($>10^3/s$).¹⁵⁾ At $t = t_0$, the workpiece material is stationary with respect to the indenter, and the constant indentation velocity (V_0) is imposed for $t_0 < t < t_0 + t_f$. For this configuration, the displacement field at $t = t_0 + t_f$, $U(y, t_0 + t_f)$, can be given by

$$\frac{U}{U_{max}} = -2\eta^2 \text{efc}(\eta) + \text{eft}(\eta) + 2 \frac{\eta}{\sqrt{\pi}} \exp(\eta^2) \quad (3)$$

where $\eta = y/\sqrt{4vt}$ is a dimensionless variable; $\text{eft}(\eta)$ and $\text{efc}(\eta)$ are the error function and complementary error function, respectively.

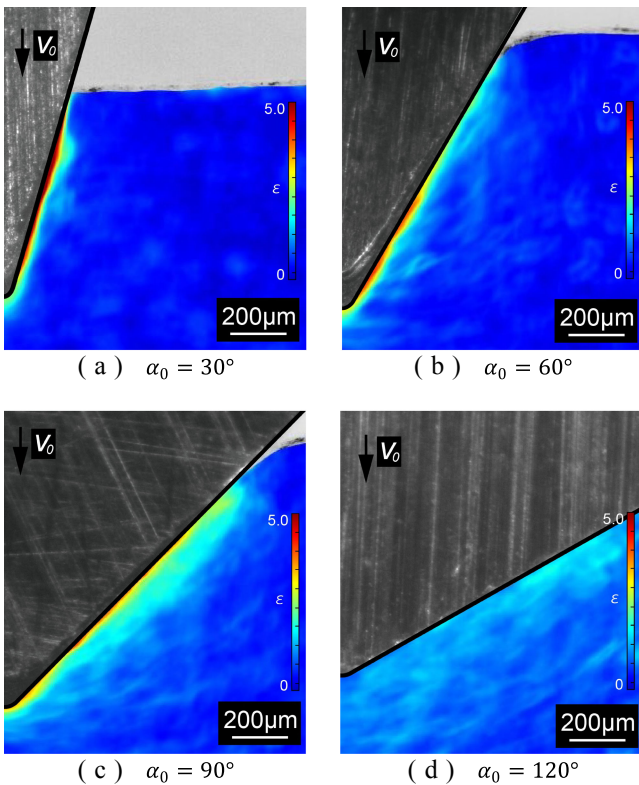


Fig. 7 Strain fields for each indenter ($t = t_0 + 0.5$ s).

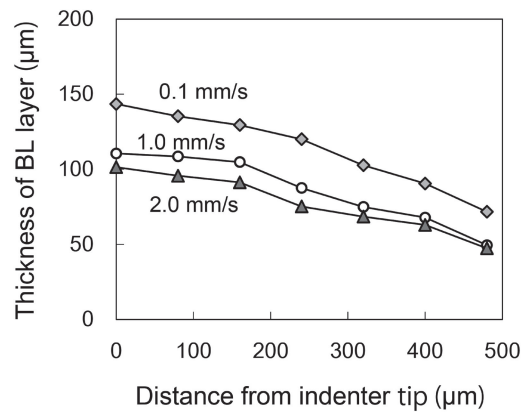


Fig. 8 Thickness of wall strained (boundary) layer along the indenter face for different indentation speeds ($\alpha_0 = 30^\circ$, $V_0 = 0.1, 1.0$ and 2.0 mm/s, $t = t_0 + 0.5$ s).

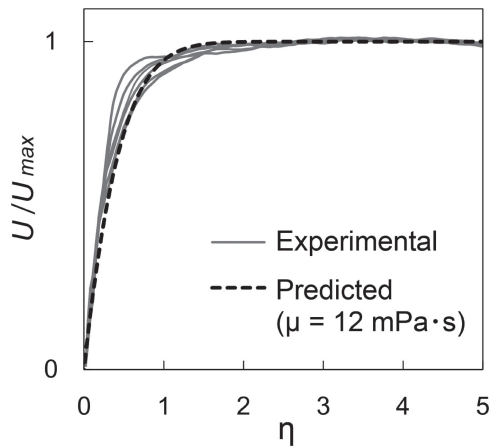


Fig. 9 Normalized displacement fields rescaled using a fitted viscosity value, and predicted curve based on the Bingham model. The displacements are plotted with respect to $\eta = y/\sqrt{4vt}$ for the narrow-angle indenters ($\alpha_0 = 30^\circ$).

Figure 9 shows the comparison between the experimentally obtained displacement fields, and that from the model described in eq. (3), as a function of $\eta = y/\sqrt{4vt}$. In this figure, the model curve was obtained by adjusting the kinematic viscous value $\nu = \mu/\rho$ (ρ : material density, and μ : dynamic viscosity), the only unknown parameter in eq. (3), to fit the experimental profiles; this curve is shown as the dotted curve. It is clear from this figure that there is good agreement between the model and experimental data for the narrowest-angle indenter wherein the cutting mode of deformation prevails. The corresponding dynamic viscosity value for the Bingham wall layer is ~ 12 mPa·s (milli-Pascal sec). This result provides strong evidence that the wall-layer with steep velocity gradients in narrow-angle indentation, where friction-induced deformation is dominant, resembles a classical fluid mechanical boundary layer and that the material flow in the layer resembles that of a Bingham-type fluid.

3.3 Influence of interface friction on boundary layer structure

Figure 10 shows the variation of indentation force with depth of penetration of the indenter ($\alpha_0 = 30^\circ$), with and without a lubricant (Polyolefin-based lubricant oils, Mobil-1). A 30% reduction of the indentation force is seen with the lubricant, indicating that the lubricant reduces the interface friction. Figure 11 shows the normalized (measured) displacement fields and the corresponding model curve fit for indentation with the lubricant. Again, the model curve agrees well with the experimental result, indicating the existence of the Bingham-type plastic boundary layer. Furthermore, the μ value of 7 mPa·s that fit the experimental profile under the lubricated condition is somewhat smaller than that obtained for the dry condition (12 mPa·s). This suggests that the friction-induced deformation becomes more localized in the lubricated case, resulting in smaller energy dissipated in the workpiece material during the indentation process. These results reinforce the notion that the friction condition at the interface changes the friction-induced deformation fields and the corresponding boundary layer

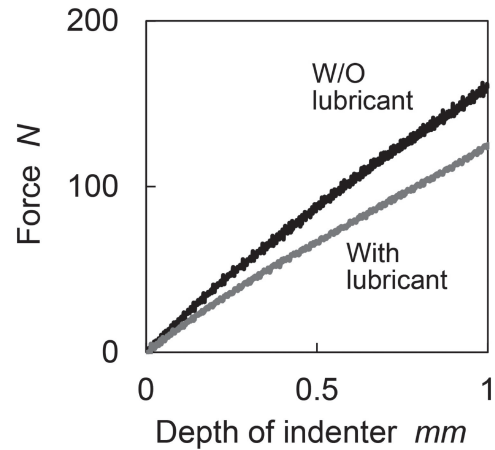


Fig. 10 Variation of indentation force with penetration (cross-head) depth, with and without a lubricant applied ($\alpha_0 = 30^\circ$).

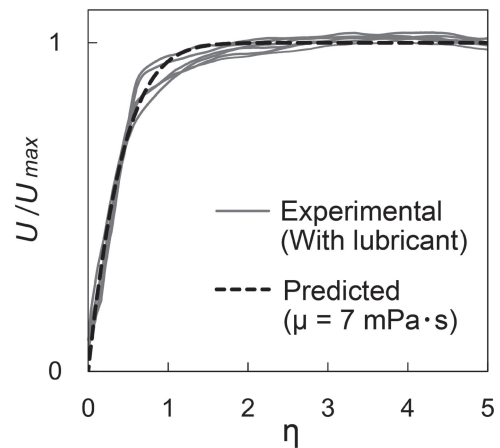


Fig. 11 Normalized displacement fields and predicted curve in the presence of lubricant ($\alpha_0 = 30^\circ$, $t = t_0 + 0.5$ s).

structure; and that this difference in the flow condition is captured by the Bingham viscosity value. Therefore, the viscosity values in eq. (2) reflect the nature of the interaction at the indenter-material interface and may be used as a discriminatory parameter for evaluating the interface friction effects.

It is noteworthy that a small amount of slip at the indenter-material interface could also be confirmed visually especially under the lubricated condition, which is currently ignored. This suggests that the lubricant affects not only the friction-induced deformation, but also the amount of slip at the interface. In contrast, in a fluid, wall slip typically does not occur, i.e., the no-velocity discontinuity boundary condition at the liquid-solid interface. Therefore, it would be of value to consider the amount of slip at the interface wall, and investigate its relation to interface friction, deformation fields and plastic boundary layer structures. This would help in establishing, rigorously, if these plastic flow fields near the wall indeed constitute a boundary layer in the fluid mechanical sense. Additional observations, with a higher resolution objective lens, are planned in the future to quantitatively evaluate the slip amount at the interface and the wall displacement fields.

4. Conclusion

An *in situ* study of flow dynamics in wedge indentation of aluminum has been performed using high-speed imaging and image correlation analysis. This has enabled quantitative characterization of deformation fields in the vicinity of the indenter-specimen interface. The material flow patterns obtained for different indenter angles clearly demarcated key features of the material flow phenomena, including the transition from a cutting of deformation to a radial-compression mode, as the indenter angle increased.

The measured displacement fields close to the indenter wall for narrow-angle indenters, where friction-induced deformation was dominant, were found to be well-described by a Bingham-solid type plastic flow model. Importantly, the wall-layers of high-strain showed strong similarity with boundary layer pattern for a Bingham solid. This suggests the existence of a plastic boundary layer adjoining the indenter wall with a characteristic viscosity. Additionally, the experiments carried out under two different lubrication conditions showed that the friction condition at the wall changed the friction-induced deformation fields, and that the difference in the material flow could be discriminated using the effective viscosity value for the Bingham solid. Hence the Bingham viscosity values reflect the nature of the interaction at the indenter-material interface, and may well be used as a parameter for evaluating the interface friction contributions and associated dissipation.

Acknowledgments

This work was supported by JSPS KAKENHI Grant Number 18K13671; and in part by US NSF Grant DMR 1610094.

REFERENCES

- 1) M.C. Shaw: *Metal Cutting Principles*, (Oxford University Press, Oxford, 2005).
- 2) R. Ramaswami: *Int. J. Mach. Tool Des. Res.* **11** (1971) 75–83.
- 3) J.A. Bailey: *Wear* **31** (1975) 243–275.
- 4) S. Kobayashi and E.G. Thomsen: *J. Eng. Ind-T ASME* **82** (1960) 324–332.
- 5) S.P.F.C. Jaspers and J.H. Dautzenberg: *J. Mater. Process. Technol.* **121** (2002) 123–135.
- 6) F. Vollertsen, H.S. Niehoff and Z. Hu: *Int. J. Mach. Tools Manuf.* **46** (2006) 1172–1179.
- 7) P. Groche, D. Fritsche, E.A. Tekkaya, J.M. Allwood, G. Hirt and R. Neugebauer: *CIRP Ann.* **56** (2007) 635–656.
- 8) M. Merklein, J.M. Allwood, B.A. Beherens, A. Brosius, H. Hagenah, K. Kuzman, K. Mori, A.E. Tekkaya and A. Weckenmann: *CIRP Ann.* **61** (2012) 725–745.
- 9) H.F. Atala and G.W. Rowe: *Wear* **32** (1975) 249–268.
- 10) H.R. Le and M.P.F. Sutcliffe: *Wear* **244** (2000) 71–78.
- 11) D.A. Rigney and J.P. Hirth: *Wear* **53** (1979) 345–370.
- 12) D.A. Rigney: *Wear* **245** (2000) 1–9.
- 13) J.A. Schey: *Tribology in Metal Working*, (American Society of Metals, OH, 1983).
- 14) N.N. Zorev: *Metal Cutting Mechanics*, (Pergamon Press, Oxford, 1966).
- 15) P.S. Jackson and O.K. Wright: *J. Manuf. Sci. E-T ASME* **104** (1982) 358–362.
- 16) T.H.C. Childs: *Wear* **260** (2006) 310–318.
- 17) T.H.C. Childs: *J. Manuf. Sci. Eng.* **13** (1971) 373–387.
- 18) H. Yeung, K. Viswanathan, W.D. Compton and S. Chandraseker: *Proc. Natl. Acad. Sci. USA* **112** (2015) 9828–9832.
- 19) Y. Guo, W.D. Compton and S. Chandraseker: *Proc. R. Soc. London, Ser. A* **471** (2015) 1–18.
- 20) N.K. Sundaram, A. Mahato, Y. Guo, K. Viswanathan and S. Chandraseker: *Acta Metall.* **140** (2017) 67–78.
- 21) W.J. Yang: *Handbook of Flow Visualization*, (Taylor & Francis, New York, 2001).
- 22) R. Hill, E.H. Lee and S.J. Tupper: *Proc. Royal Soc. Lond.* **118** (1947) 273–289.
- 23) A.G. Atkins and D. Tabor: *J. Mech. Phys. Solids* **13** (1965) 149–164.
- 24) J.B. Haddow: *Int. J. Mech. Sci.* **9** (1967) 159–161.
- 25) A. Udupa, N. Sundaram, T. Sugihara and S. Chandraseker: *Mater. Trans.*, under review.
- 26) G. Batchelor: *An Introduction to Fluid Dynamics*, (Cambridge University Press, Cambridge, 2000).